Fuel 406 (2026) 137001

Contents lists available at ScienceDirect

Fuel

journal homepage: www.elsevier.com/locate/fuel

Full Length Article

Combustion and emission characteristics of premixed coke oven gas-ammonia swirling flames

Daisuke Sato [a,b,*], Jordan Davies [a], Sanggak Lee [a], Syed Mashruk [a], Agustin Valera-Medina [a], Ryoichi Kurose [b]

[a] College of Physical Sciences and Engineering, Cardiff University, Wales CF24 3AA, UK
[b] Department of Mechanical Engineering and Science, Kyoto University, Kyoto daigaku-Katsura, Nishikyo-ku, Kyoto 615-8540, Japan

ARTICLE INFO

Keywords:
Zero-carbon
Ammonia
Coke oven gas
Turbulent flames
NO
CO

ABSTRACT

This study systematically investigates the combustion characteristics of co-firing Coke Oven Gas (COG) and ammonia (NH_3), a promising low-carbon fuel blend for decarbonising the steel industry. Experiments are conducted using a 10 kW tangential swirl burner, varying the ammonia fraction (X_{NH3}) and equivalence ratio (Φ). Results demonstrate a significant synergistic effect, where blending expands the flame stability range; ammonia addition suppresses flashback from the high-hydrogen COG, while COG enhances the reactivity of ammonia. The widest stability range is achieved at $X_{NH3} = 0.2$. An analysis of exhaust gas emissions reveals that increasing X_{NH3} not only suppresses the peak NO concentration but also shifts the equivalence ratio at which NO concentration is negligible on the fuel-rich side closer to the stoichiometric condition. Furthermore, a Chemical Reactor Network (CRN) analysis identifies that the HNO + OH ↔ NO + H_2O reaction, promoted by OH radicals from COG, is a crucial NO formation pathway, a novel finding for this fuel blend. These fundamental data contribute to advancing the practical application of COG/NH_3 co-firing.

1. Introduction

Coke oven gas (COG) is a by-product gas generated during the carbonisation of coal in coke ovens. Historically, it was used as a primary heat source in industrial cities, such as those in the United Kingdom, to meet energy demands. Today, it remains a key fuel for industrial furnaces in steelworks that operate coke ovens [1]. While its exact composition varies with the coal type and carbonisation process, COG typically consists of 55–65 vol% hydrogen (H_2), 23–30 vol% methane (CH_4), 5–8 vol% carbon monoxide (CO), 2–4 vol% carbon dioxide (CO_2), and 3–6 vol% nitrogen (N_2), along with trace amounts of higher hydrocarbons such as ethane and ethylene [1–3]. This high hydrogen content results in a significantly faster burning velocity than that of conventional fuels like natural gas, making COG susceptible to flashback [4,5]. While the above are the characteristics of refined COG used in industrial furnaces, raw COG from coke ovens contains traces of ammonia as a by-product [1–3]. This ammonia can be considered a resource rather than a mere impurity. As evidence, several recent studies [6–8] have conducted life cycle assessments of routes to recover this ammonia from raw COG as a zero-carbon energy carrier, highlighting its potential as a valuable resource. This presents a unique opportunity: rather than expending energy to remove the ammonia (current practice) or to extract it for separate use, it can be combusted directly within the COG stream. Co-firing raw COG with additional ammonia could therefore potentially eliminate purification costs, improve combustion stability, and contribute to decarbonising the steel industry, which is responsible for 5–7 % of global anthropogenic CO_2 emissions [9].

This concept aligns with the growing global interest in ammonia as a carbon-free energy carrier, particularly for storing and transporting renewable energy. Compared to hydrogen, ammonia can be liquefied under much milder temperature and pressure conditions, which allows for more cost-effective storage and transport. Furthermore, researchers are increasingly investigating green ammonia derived from renewable sources with no CO_2 emissions upon combustion not only as an energy carrier but also as a direct fuel [10,11]. However, the use of ammonia as a fuel presents challenges, including poor flame stability due to its low reactivity and burning velocity, as well as nitrogen oxide (NOx) emissions under conventional furnace operating conditions [12,13].

As noted, COG's high burning velocity creates a risk of flashback, while ammonia's low burning velocity leads to a risk of flame blow-off. Blending these two fuels may therefore balance these contrasting

* Corresponding author at: College of Physical Sciences and Engineering, Cardiff University, Wales CF24 3AA, UK.
E-mail address: satod@cardiff.ac.uk (D. Sato).

https://doi.org/10.1016/j.fuel.2025.137001
Received 6 August 2025; Received in revised form 16 September 2025; Accepted 27 September 2025
Available online 1 October 2025

Nomenclature

COG	Coke Oven Gas
LBO	Lean Blowout
RBO	Rich Blowout
FB	Flashback
CRN	Chemical Reactor Network
PFR	Plug Flow Reactor
PSR	Perfectly Stirred Reactor
FZ	Flame Zone
CRZ	Central Recirculation Zone
ERZ	External Recirculation Zone
PFZ	Post Flame Zone
ROP	Rate of Production
LBV	Laminar Burning Velocity
MFC	Mass Flow Controller
Φ	Equivalence Ratio
XNH3	Ammonia Fraction
Sg	Geometric Swirl Number

properties, overcoming their individual drawbacks to achieve stable combustion [14]. This potential for synergy makes COG/NH_3 co-firing a promising future fuel for industrial furnaces in steelworks.

Numerous studies have investigated the co-firing of ammonia with other fuels. For NH_3/H_2 blends, previous studies [15–21] have shown that adding hydrogen improves the burning velocity and widens the flammability limits, though NOx emissions tend to increase at high hydrogen fractions. Research on NH_3/CH_4 flames [22–26] reveals similar trends, but this mixture exhibits other complex behaviours, including a non-linear relationship between the CH_4 fraction and NOx emissions, as well as the production of CO. Han et al. [27] experimentally measured the burning velocities of NH_3 blended separately with H_2, CO, and CH_4, clarifying the effects of varying blend and equivalence ratios.

However, for the co-firing of NH_3 with the multi-component fuel COG, key knowledge gaps remain regarding both flame stability and the emission of pollutants like NOx and CO, which are critical for industrial applications. A simulation study by Kekul et al. [14] on COG/NH_3 flames, both with and without steam, suggested that increasing the COG ratio enhances the Laminar Burning Velocity (LBV) and flame temperature but also increases NO emissions. Experimentally, Yang et al. [28] measured the LBV of COG/NH_3 flames and demonstrated through kinetic analysis that adding COG significantly enhances the LBV via combined chemical and thermal effects.

Key studies by Hewlett et al. [29,30] investigated COG/NH_3 swirl combustion using both simulations and experiments. Their work on blends of COG with anhydrous ammonia (AA) or ammonia vapor (AV) suggested an optimal NH_3 fraction (X_{NH3}) of 0.85 for minimising pollutant emissions, a finding confirmed in both their models and experiments. However, these important studies by Hewlett et al. [29,30] focused on conditions near the optimal ammonia fraction for minimizing emissions ($X_{NH3} = 0.85$), leaving several key knowledge gaps. First, due to the limited experimental conditions, a comprehensive flame stability map covering a wider range of equivalence ratios and higher COG fractions was not presented. This left the full picture of the synergistic effect on stability namely, how ammonia addition suppresses flashback from the high hydrogen COG, and how COG enhances the poor reactivity of ammonia unclarified. Second, a detailed kinetic analysis of the elementary reactions governing pollutant formation and destruction, particularly the influence of COG's multicomponent nature including inert gases like CO_2 and N_2, had not been performed. Therefore, this study aims to fill these knowledge gaps. Using a COG composition that includes inert gases to more closely resemble actual industrial by-product gas, this study systematically investigates the combustion stability and emission characteristics over a wide range of ammonia fractions ($0 \leq X_{NH3} \leq 0.9$) and equivalence ratios. Furthermore, by conducting a detailed chemical kinetic analysis to identify the key reaction pathways for pollutant formation, especially the unique NOx formation mechanisms for this specific fuel blend, this work provides fundamental data to advance its practical application.

2. Experimental setup and methodology

2.1. Tangential swirl burner

The tangential swirl burner used in this study and its peripheral equipment are shown in Fig. 1. All combustion experiments were conducted under atmospheric pressure conditions (1.1 bar). COG, NH_3, and Air were injected into a premixing chamber at ambient temperature (288 K) and then passed through a tangential swirler to form a swirl flame with a geometric swirl number (Sg) of 1.45. In this study, a stable gas composition close to the actual COG composition was adopted based on previous literature [29,30]. This COG was mixed with ammonia, and the combustion characteristics were investigated in the range of ammonia volume fraction $0 \leq X_{NH3} \leq 0.9$, as shown in Table 1. Bronkhorst flow controllers (accuracy ± 0.5 % full scale) were used to regulate the flow rates of NH_3 and Air, while an ALICAT mass flow controller (accuracy ± 0.2 % full scale) was used for the COG. All experimental conditions were maintained at a constant power of 10 kW. Furthermore, the combustion region above the burner was enclosed by a GE214 quartz tube (d = 156 mm), which is 85 % transparent over the wavelength range required for the chemiluminescence measurements in this study.

As stated in Section 1, the actual composition of COG varies depending on the type of coal and the carbonisation conditions. However, based on previous studies [29,30], this research utilised a simplified gas composition that only omitted C_2H_4 and C_2H_6, which together account for approximately 2.2 vol%.

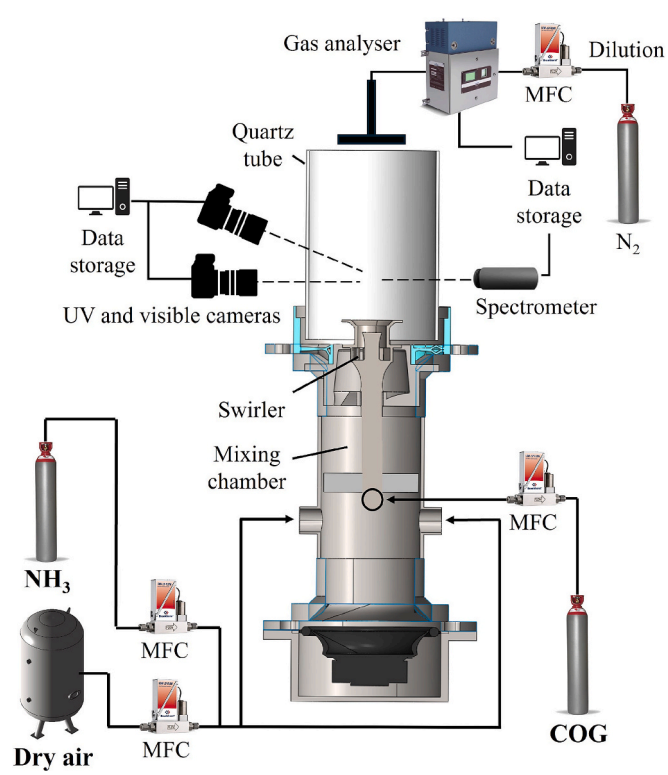

Fig. 1. Schematic of experimental system.

Table 1
Fuel compositions (mole fraction).

Blend No.	X_{NH3}	X_{H2}	X_{CH4}	X_{CO}	X_{CO2}	X_{N2}
1	0.9000	0.0622	0.0247	0.0072	0.0019	0.0040
2	0.8500	0.0933	0.0371	0.0108	0.0029	0.0060
3	0.8000	0.1244	0.0494	0.0144	0.0038	0.0080
4	0.6000	0.2488	0.0988	0.0288	0.0076	0.0160
5	0.4000	0.3732	0.1482	0.0432	0.0114	0.0240
6	0.2000	0.4976	0.1976	0.0576	0.0152	0.0320
7	0.0000	0.6220	0.2470	0.0720	0.0190	0.0400

In this study, the combustion limits for the specific burner and fuel combination were first investigated by varying the equivalence ratio (Φ) over a range of NH_3 volume fractions in the COG/NH_3 fuel blends ($0.0 \leq X_{NH3} \leq 0.9$). This range included $X_{NH3} = 0.85$, which yielded the lowest NO emission concentration in a previous study [29]. Subsequently, for each X_{NH3}, exhaust gas composition analysis and chemiluminescence measurements were performed for $0.6 \leq \Phi \leq 1.4$, within the operational range that avoided lean blowout (LBO), rich blowout (RBO), and flashback (FB).

2.2. Measurements methods

2.2.1. Exhaust gas emission analysis

The concentrations of exhaust gas species (NO, N_2O, NO_2, NH_3, O_2, CO, and H_2O) were analysed at a frequency of 1 Hz using an Emerson CT5100 Quantum Cascade Laser analyser (reproducibility ± 1 %, linearity $R^2 > 0.999$). To ensure uniform sampling from the entire exhaust gas stream, the sample gas was extracted through evenly spaced holes in a cruciform probe located at the outlet of the quartz tube. The sample line was heated to 463 K to prevent condensation. When the concentration of a component exceeded the analyser's detection limit, the sample was diluted with N_2 before measurement, as described in previous work [31]. This dilution method was applied with a repeatability of ± 10 %. All emission data in this paper are reported as 120-second time-averaged values, normalised to 15 % O_2 (dry) condition in accordance with British standards [32].

2.2.2. Chemiluminescence measurements

A fibre optic spectrometer (AvaSpec-ULS4096CL-EVO) was positioned at an axial distance of 40 mm above the burner exit to measure the chemiluminescence from radicals actively involved in the combustion reactions within the flame zone. The spectrometer, featuring a high spectral resolution of 0.3 nm and a sensitive range of 200 nm to 1100 nm, is capable of accurately detecting narrow spectral signals. Additionally, the spectrometer was placed at a radial distance of 350 mm from the quartz cylinder to minimise thermal exposure and optical distortion caused by the high-temperature gradients near the burner. The exposure time was set to 1 s, and 20 scans were averaged to improve the signal-to-noise ratio (SNR). A Y-axis calibration using a standard light source (SL1 tungsten-halogen) ensured quantitative accuracy and consistency throughout all measurements. To evaluate the intensity of a single species of chemiluminescence from the spectral data over a wide range of measured wavelengths, spectral integration was performed over the wavelength range corresponding to each radical's chemiluminescence. The wavelength ranges were set as follows [33–37]: OH* 302–326 nm (A2Σ + − X2Π system), NH* 335–346 nm (A3Π − X3Σ − system), NH_2* 620–645 nm (the part of NH_2 α band), C_2* 510–520 nm (A3Πg–X3Πu system) [33], and CH* 429–443 nm (A2Δ − X2Π system). Before performing the spectral integration, broadband background subtraction from H_2O* and CO_2* was carried out using the method described by Zhu et al. [38] and Mashruk et al. [39] The detailed procedure is described in their papers.

In addition, various chemiluminescence images were acquired at a frequency of 10 Hz using multiple LaVision cameras, each equipped with a Sony ICX285AL sensor and a Hamamatsu HB105831 intensifier. These measurements utilised Edmund Optics bandpass filters with a 10 nm FWHM, centred at 310 nm, 337 nm, 430 nm, 515 nm, and 632 nm. These filters correspond to the emissions of OH* (309 nm), NH* (336 nm), CH* (430 nm), C_2* (516 nm), and NH_2* (630 nm), respectively. For each test point, the raw images were processed in LaVision Davis v10 by applying background image subtraction, a 3x3 pixel median filter, and time-averaging over 200 frames. Subsequently, Abel deconvolution was performed on the processed images [40]. All chemiluminescence images in this paper were normalised by the maximum intensity of its respective radical, showing the right half of the flame.

Furthermore, direct line of sight images of the flame were captured using Nikon Z7ii mirrorless digital camera to observe its stability behaviour. The camera was set to an aperture of F/4, an exposure time of 1/3 s, and ISO of 64.

2.2.3. Chemical kinetic modelling

To identify the key reactions involved in emission formation, analyses were conducted at X_{NH3} = 0.6, 0.8, and 0.9 using a Chemical Reactor Network (CRN) previously used in CHEMKIN-PRO [31,41–43]. In this CRN, as illustrated in Fig. 2, the swirl flame is modelled by connecting Perfectly Stirred Reactors (PSRs) which represent the mixing zone, Flame Zone (FZ), Central Recirculation Zone (CRZ), and External Recirculation Zone (ERZ), and a Plug Flow Reactor (PFR) representing the Post Flame Zone (PFZ). In this study, a novel and simple method is proposed and validated for defining the respective reaction zones of the CRN from chemiluminescence images, which are relatively easy to measure. The PSR volume values for the FZ, CRZ, and ERZ, which are directly linked to the residence time within the PSR, were calculated from NH_2* chemiluminescence images based on the geometrical assumptions shown in Fig. 3. NH_2* chemiluminescence was selected because it is emitted during the initial, low-reactivity stage of ammonia combustion and from a broader area than other radical chemiluminescence. This supports the reasonable assumption, consistent with previous studies [44,45], that its emission region covers the entire FZ. These geometrical assumptions for defining the volume of each zone are consistent with findings from previous experimental and numerical study [41]. Specifically, the area where brightness exists due to the binarization process (area surrounded by a red dashed line in Fig. 3) was first assumed to be the FZ area. Multiple points on the left side of the FZ area, including the vertices, were obtained as reference points (light blue points in Fig. 3). The central area surrounded by the approximation line of the reference points and the line obtained by horizontally inverting the approximation line around the vertex of the FZ area was assumed to be the CRZ. The ERZ was defined based on a model of the physical flow behaviour. In a swirl flame, the hot gas jet continues to flow forward towards the combustor wall even after it ceases to be luminous. It is assumed that this flow impinges on the wall and is then partially entrained downwards, forming the external recirculation. To model the volume where this recirculation originates, the boundary of this forward-flowing jet was first identified. An approximation curve of

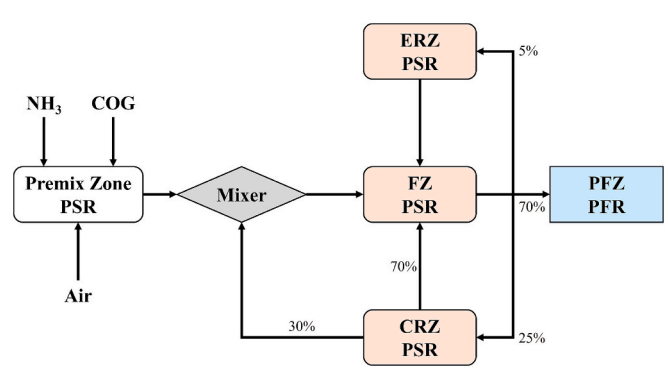

Fig. 2. Schematic of chemical reactor network.

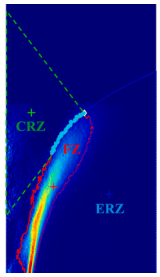

Fig. 3. Zone discrimination map using NH_2* chemiluminescence image (Example of $X_{NH3} = 0.6$, $\Phi = 1.0$).

the reference points on the FZ contour was created and then extrapolated along the main flow direction to the right-hand wall. This extrapolated line represents the upper boundary of the non-luminous hot gas jet. The region below this extrapolated line and outside of the FZ was consequently defined as the ERZ, representing the zone where the forward flow turns to become the recirculation flow. The CRN areas, identified using the method described above, showed that as X_{NH3} increased from 0.6 to 0.8, the FZ and ERZ expanded by 19 % and 11 %, respectively, while the CRZ shrank by 35 %. This result is consistent with the data presented later in Fig. 8(b). The expansion of the flame region is attributed to the increased concentration of less reactive ammonia. The reduction of the CRZ area is a consequence of the overall flame narrowing. The recirculation intensity was determined by previous experiments that employed comparable swirl burners [41]. In prior experimental study, the velocity field of the swirling flow downstream of the burner was measured in detail using Laser Doppler Anemometry (LDA), a non-intrusive optical technique, which allowed for the quantitative evaluation of the recirculation rate.

In this study, NO and CO concentration outputs were compared and evaluated using three mechanisms. First, GRI-Mech 3.0 [46] was chosen as a fundamental basis for comparison, as it is a well-validated and established benchmark in the field of natural gas combustion and includes elementary reactions for the main components of COG. Next, the mechanism from Okafor et al. [47] was selected because it was specifically developed for the combustion of CH_4/NH_3 mixture. This mechanism was expected to describe the interaction between CH_4 and NH_3 with high accuracy. Furthermore, focusing on the fact that the COG in this study is a hydrogen-rich fuel containing over 60 % H_2, the well-established mechanism from Li et al. [48] was also adopted. Of course, other detailed mechanisms for CH_4, H_2, and NH_3 exist. However, this study also considers future applications in CFD analysis, which requires a balance between computational cost and predictive accuracy. Therefore, the three mechanisms were deemed the most appropriate for achieving the objectives of this research, as they do not involve an excessive number of reactions or chemical species.

Subsequently, using the mechanism with the highest predictive accuracy, a Rate of Production (ROP) and sensitivity analysis was performed to assess the contribution of elementary reactions to the formation and consumption of NO and CO. The analysis focused on the conditions of $X_{NH3} = 0.6$ and 0.8 at $\Phi = 1.0$. While NO concentrations typically peak under lean conditions and CO concentrations under rich conditions, an equivalence ratio of $\Phi = 1.0$ was specifically chosen for this analysis. The objective was not merely to identify the dominant reactions for each species at its peak concentration, but rather to elucidate the competing reactions that govern the production and consumption of both NO and CO simultaneously. In practical combustor applications, identifying operating windows where both pollutants can be kept low is critically important. Therefore, selecting a condition where both NO and CO are generated is reasonable for investigating the trade-offs and interactions between their respective chemical pathways.

3. Results and discussion

3.1. Stability limit

The stability map for a fixed condition of 10 kW in the swirl burner and fuel compositions of this study is shown in Fig. 4. The LBO limit, RBO limit, and FB limit for each X_{NH3} are plotted, and the grey hatched area enclosed by the plots indicates the flame stability range. It should be noted that for $X_{NH3} = 0$ and 0.2, the lower flame stability limit below an equivalence ratio of 0.35 could not be confirmed due to the air supply limitation of the mass flow controller.

From this stability map, it was confirmed that for pure COG, the flame stability range on the rich side is extremely narrow, with flashback occurring at $\Phi = 1.1$. This is thought to be because the swirl burner used in this study was designed for high ammonia fraction blend combustion [49], which has a slow burning velocity. Consequently, for pure COG, the burner outlet cross-sectional area is large, and under rich conditions, the flow velocity is too low relative to the burning velocity [5]. In contrast, at $X_{NH3} = 0.2$, the flame stability limit range under rich conditions expanded significantly, and a flame was formed up to $\Phi = 2.05$. On the lean side, LBO did not occur down to $\Phi = 0.35$, which is the supply limit of the air mass flow controller (MFC), revealing that the blend with the widest stability range in this study is $X_{NH3} = 0.2$. This signifies that the complementary enhancement of reactivity through the mixing of COG and NH_3, as mentioned in Section 1, is effective, demonstrating that the expected synergy is indeed realised. Furthermore, it was confirmed that as the NH_3 fraction is decreased from $X_{NH3} = 0.9$ (i.e., the COG fraction is increased), the LBO equivalence ratio limit gradually decreases, and the RBO equivalence ratio limit sharply increases, thereby expanding the stability range up to $X_{NH3} = 0.2$. This is presumed to be due to the thermal effect (increase in flame temperature) and the enhancement of reactivity by promoting the production of OH radicals from COG addition, as shown in previous literature [28] using simplified COG ($H_2/CH_4/CO$). Although the COG used in this study, which closely resembles the composition of actual by-product gas, contains inert gases such as CO_2 and N_2, these results reveal for the first time that the combustion stabilisation effect due to enhanced reactivity surpasses the dilution effect of these inert gases.

Next, to discuss combustion stability in more detail, photographs of COG/NH_3 swirl flames near the flame stability limit and in stoichiometric conditions are shown in Fig. 5. First, under stoichiometric conditions (middle row of Fig. 5), the entire flame elongated downstream as the NH_3 fraction increased. Furthermore, a gradual change in the flame's luminescence from blue to orange was observed. This trend was

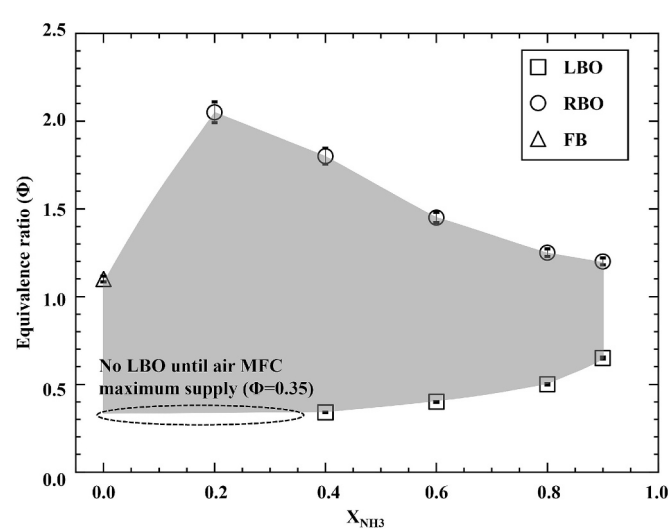

Fig. 4. Stability map of COG/NH_3 swirl flame (10 kW power constant).

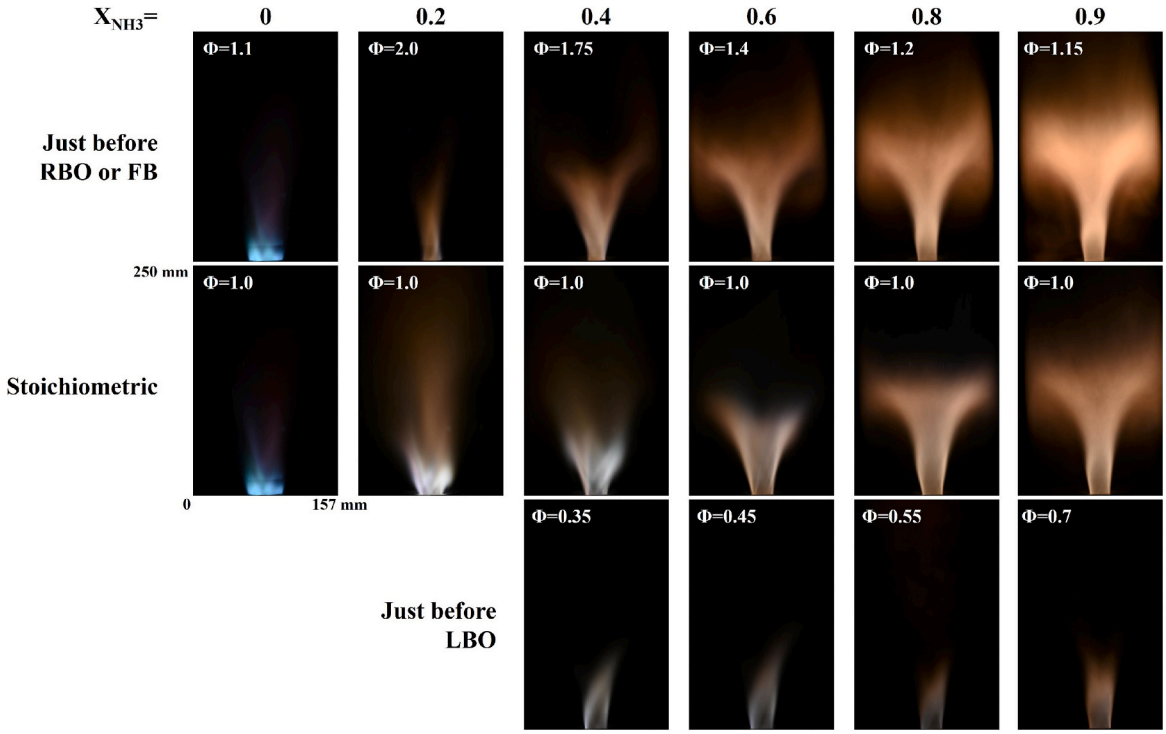

Fig. 5. Photographs of COG/NH_3 swirl flames near the flame stability limit and in stoichiometric conditions.

consistent with the results of previous studies on NH_3/CH_4 [50] and $NH_3/H_2/CH_4$ [51] blends. Just before LBO, as shown in the bottom row of photographs in Fig. 5, it was observed that the upper part of the flame was blown off due to an excessive supply of air, leaving only the flame base. When the equivalence ratio was further decreased from the conditions in the bottom photographs (by increasing the air flow rate), the remaining flame base could no longer be sustained and was extinguished. In contrast, just before RBO, as shown in the top row of photographs in Fig. 5, the upper part of the flame remained until the last moment, but when the equivalence ratio was further increased (by decreasing the air flow rate), the thinning flame base tore off, and the flame was blown out.

In summary, it was suggested that for high-COG fraction fuels, the flashback suppression effect due to ammonia addition makes a significant contribution to expanding the stability range. In contrast, for high-NH_3 fraction fuels, it was suggested that the enhancement of reactivity

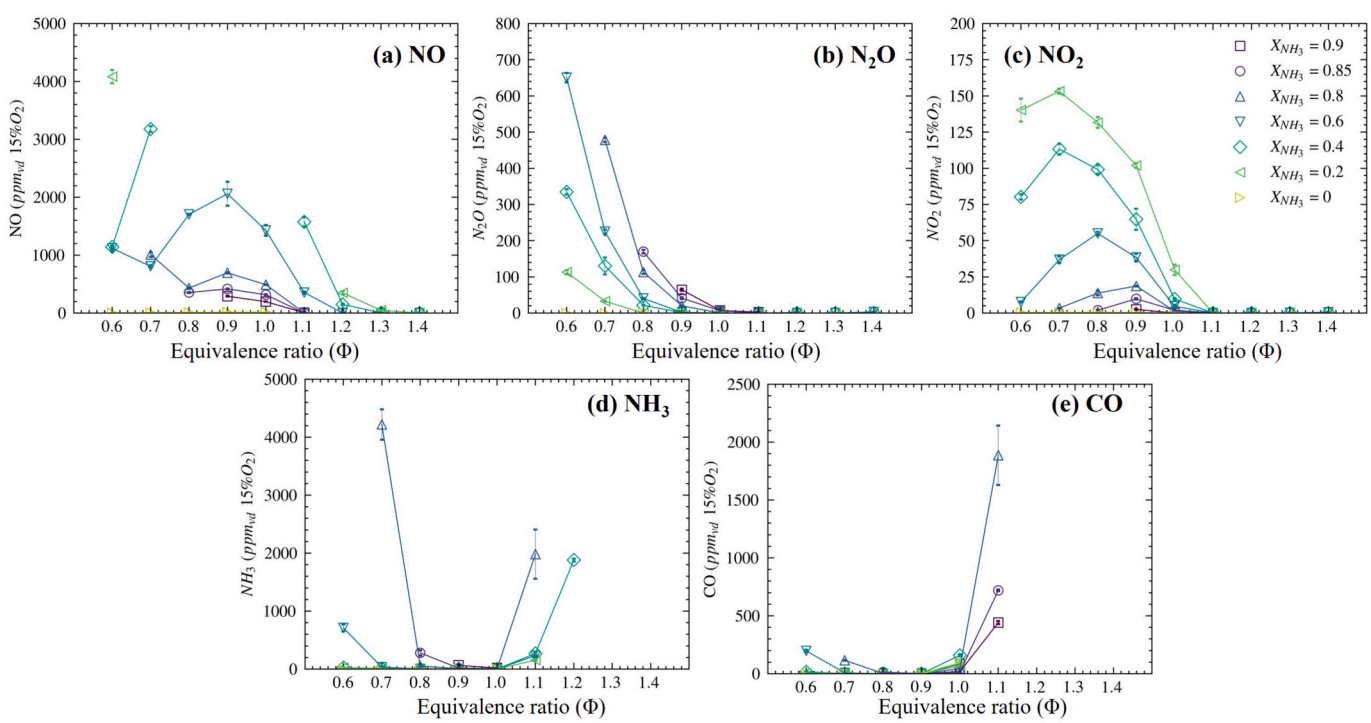

Fig. 6. Exhaust gas concentration of (a) NO, (b) N_2O, (c) NO_2, (d) NH_3, (e) CO at 10 kW constant power.

due to the thermal and chemical effects of COG addition makes a significant contribution to expanding the stability range. In addition, the respective occurrence behaviours of LBO and RBO were clarified. The flame stability of COG/NH_3 swirl flames with a COG composition extremely close to actual COG, including the inert gases CO_2 and N_2, was evaluated for the first time in this study. These results are expected to make a significant contribution to future burner design.

3.2. Exhaust gas emission analysis

The graphs plotting the exhaust gas concentrations for each COG/NH_3 condition are shown in Fig. 6. All concentrations were output after being corrected to a dry 15 % O_2 basis.

First, the NO concentration showed a tendency to decrease as X_{NH3} increased overall, except for the pure COG. As a result, the equivalence ratio at which the NO concentration fell to a negligible level shifted on both the lean and rich sides with the change in X_{NH3}, thereby narrowing the equivalence ratio range for NO emissions. Furthermore, at X_{NH3} = 0.6, 0.8, and 0.85, the concentration tended to peak around $\Phi = 0.9$. It is considered that a high COG fraction increases the flame temperature and promotes the generation of radicals such as OH, thereby increasing NO concentration. A detailed kinetic analysis is discussed in Section 3.4.

Regarding N_2O, the concentration was negligible at $\Phi = 1.0$ and above. However, a sharp increase in concentration was observed under lean conditions. Furthermore, higher X_{NH3} levels resulted in increased N_2O emissions, which in turn caused a corresponding increase in the equivalence ratio for negligible N_2O concentrations. Based on the paper by Mashruk et al. [31], it is presumed that this phenomenon is caused by a decrease in the H_2 fraction and flame temperature within the flame.

Similar to NO, NO_2 showed a tendency to decrease as X_{NH3} increased, but it was confirmed that its peak position shifted slightly toward the side with a smaller equivalence ratio as X_{NH3} increased. In addition, the equivalence ratio at which the NO_2 concentration was a negligible level shifted on both the sides with smaller and larger equivalence ratios as X_{NH3} changed, thereby narrowing the equivalence ratio range for NO_2 emissions. Also, the NO_2 concentration was significantly smaller than that of NO, reaffirming that NO is the main component of NOx.

For NH_3, the concentration was almost zero at $\Phi = 0.9$ and 1.0 for all X_{NH3} levels. However, it was confirmed that the unburned NH_3 concentration increased sharply with an increase or decrease in the equivalence ratio. It was also clarified that the higher the X_{NH3}, the narrower the equivalence ratio range where unburned NH_3 concentration are low. This correlates with the stability map in Fig. 4, and it is presumed that ammonia slip occurred due to combustion instability under conditions close to the stability limits on the fuel rich and lean sides.

CO concentration showed a tendency to increase sharply, particularly on the fuel rich side. This increase was more rapid under conditions with lower X_{NH3} (higher carbon content in the fuel), and with blends of $X_{NH3} = 0.6$ or less, the concentration exceeded the upper detection limit of the gas analyser at $\Phi = 1.1$. On the lean side, some CO was also detected due to combustion instability, but the increase was not as pronounced as that of the NH_3 concentration.

3.3. Chemiluminescence measurement

To further understand the combustion characteristics, chemiluminescence was measured, focusing on the conditions of X_{NH3} = 0.6–0.9, where NO emissions were low as shown in Fig. 6. The chemiluminescence intensity of each radical, as measured by a spectrometer, was normalised by its maximum value and is shown in Fig. 7. Furthermore, Fig. 8 shows the images of chemiluminescence for OH*, NH_2*, NH*, C_2*, and CH*.

First, it was found that the OH* chemiluminescence intensity increases significantly at low X_{NH3} (high X_{COG}) and around $\Phi = 0.9$. This trend is consistent with previous research on ammonia blend combustion [38,52]. This is thought to be because hydrogen derived from COG, the precursor to OH*, becomes abundant in the combustion field, and moreover, the flame temperature increases. The image in Fig. 8(a)

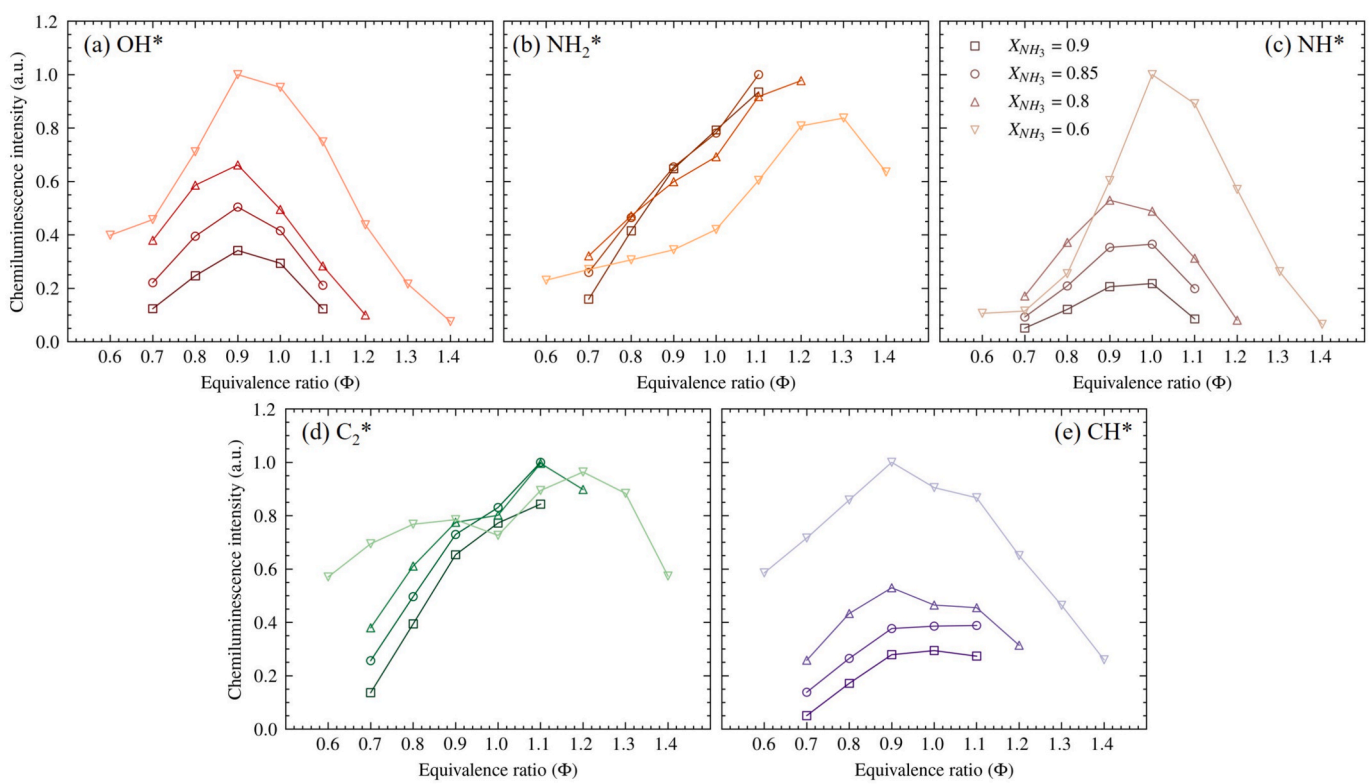

Fig. 7. Measured chemiluminescence intensities of single excited radicals at 10 kW constant power. Within each subplot, the different colour shades and marker styles represent the X_{NH3} defined in the common legend shown in panel (c).

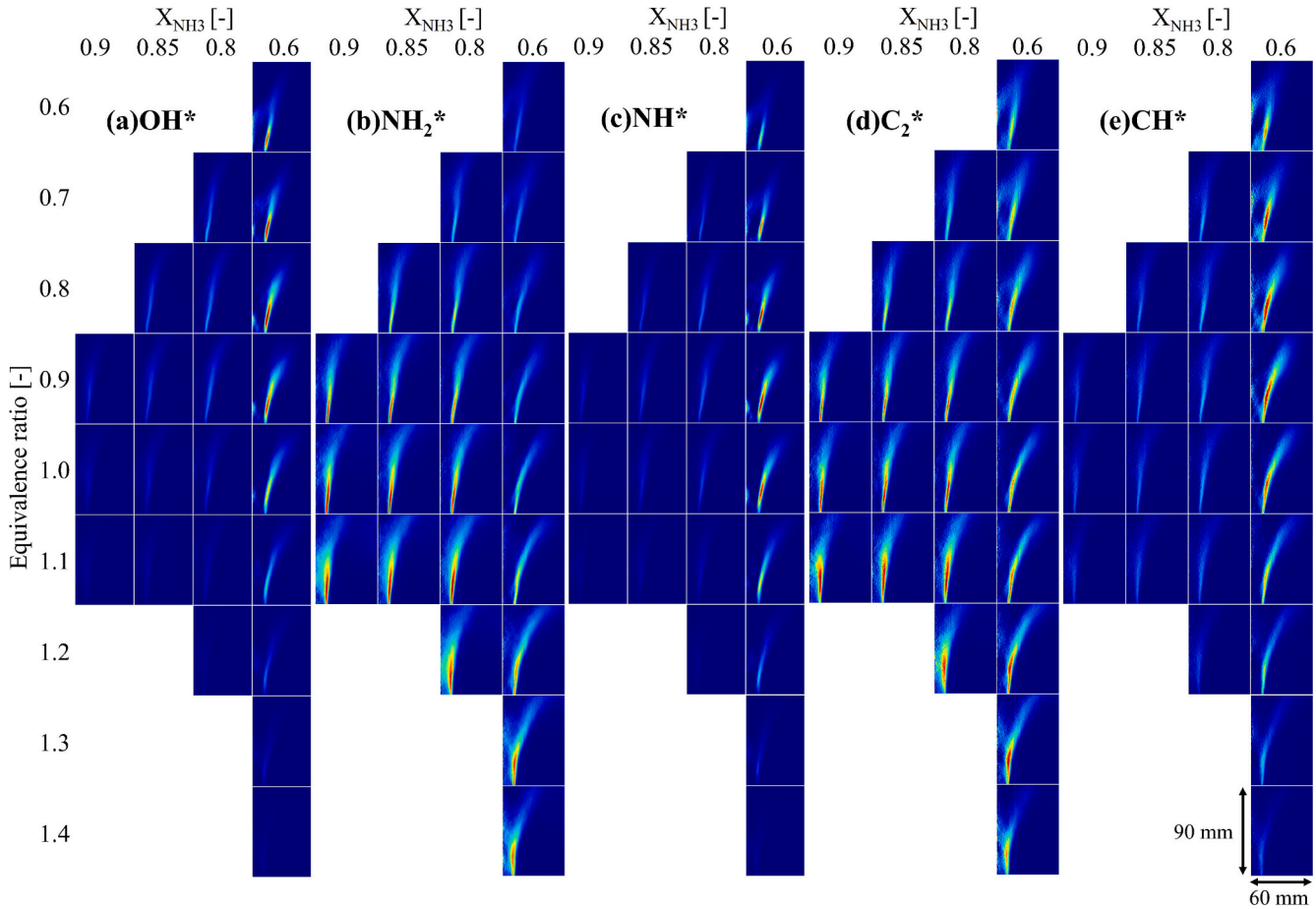

Fig. 8. Chemiluminescence images of each radical at 10 kW constant power.

suggests that, compared to other chemiluminescence, the emission is narrowly distributed in the central part of the flame, which is useful for identifying the high temperature region where combustion reactions are active.

In contrast, the NH_2* chemiluminescence was found to increase in intensity and be widely distributed at high X_{NH3} (low X_{COG}) and high equivalence ratios (rich conditions). Previous studies [53,54] on NH_3 flames have cited the initial combustion reaction $NH_3 + H \leftrightarrow NH_2^* + H_2$ as the primary formation reaction for NH_2*. The increase in NH_2* intensity with increasing X_{NH3} is thought to be caused by an increase in fuel derived NH_3 and H. The intensity increase at high equivalence ratios (rich conditions) is considered to be because the consumption of H by oxidisers in the combustion field is reduced, leading to an increase in the $NH_3 + H \leftrightarrow NH_2^* + H_2$ reaction.

Additionally, the NH* chemiluminescence was found to increase significantly at low X_{NH3} (high X_{COG}) and around $\Phi = 0.9$, exhibiting a trend like that of OH*. This result seems counterintuitive to the expectation that more ammonia derived NH* would be produced under high X_{NH3} conditions. However, previous study [55] have identified reactions such as $NH_2 + OH \leftrightarrow NH^* + H_2O$ and $NH_2 + H \leftrightarrow NH^* + H_2$ as formation pathways for NH*, which depend not only on the concentrations of NH_3 and NH_2 in the combustion field but also significantly on the flame temperature. In other words, these measurement results suggest that the NH* chemiluminescence was strongly influenced by the increase in flame temperature resulting from a high COG content and an equivalence ratio approaching $\Phi = 0.9$.

Furthermore, it has been revealed that C_2* chemiluminescence has a smaller difference in intensity between blends compared to other radicals, and has a reasonable intensity even under high X_{NH3} conditions (conditions with less COG). In addition, it has been clarified that C_2* chemiluminescence has a peak particularly under fuel rich conditions ($1.1 \leq \Phi$). In past research [56], $CH_2 + C \leftrightarrow C_2^* + H_2$ has been cited as the main generation reaction of C_2*, and the original CH_2 and C are generated by the decomposition of CH_4 contained in COG. Therefore, the emission intensity becomes high under fuel rich conditions where the oxidant derived from air is insufficient and the pyrolysed CH_2 and C become abundant in the combustion field. In addition, its emission position is useful for identifying the complete thermal decomposition position of CH_4, and the results shown in Fig. 8 (d) suggest that thermal decomposition is active inside the flame under all conditions, and the intensity at the flame tip is small, suggesting that the decomposition has already been completed. Interestingly, a valley of intensity around the stoichiometric condition was confirmed as a tendency peculiar to $X_{NH3} = 0.6$. This is a feature that becomes evident by excluding the broad CO_2* chemiluminescence. Under this condition, since the flame temperature and the concentration of oxidising radicals (O, OH) become high, it is presumed that although C_2 precursors (CH, C, etc.) are generated, they are rapidly oxidised into CO and CO_2 before they have chance to form C_2. This oxidation pathway likely becomes dominant due to the high flame temperature and concentration of oxidizing radicals (O, OH) under the conditions.

Finally, the CH* chemiluminescence was found to increase significantly at low X_{NH3} (high X_{COG}) and low equivalence ratios (lean conditions). Its emission distribution is similar to that of OH* and NH*, but it is characterised by a thicker emission band in the flame. Although for other fuels, previous study [55] have shown that the reactions $C_2 + OH \leftrightarrow CH^* + CO_2$, $C_2H + O_2 \leftrightarrow CH^* + CO_2$, and $C_2H + O \leftrightarrow CH^* + CO$ are strongly related to CH* chemiluminescence. From this, it is inferred that the CH* chemiluminescence intensity was enhanced under conditions where C_2 and C_2H (resulting from a high hydrocarbon fuel ratio) and

OH, O_2, and O (resulting from a low equivalence ratio) are all abundant in the combustion field. Additionally, Mashruk et al. and Zhu et al. [39,57] investigated the chemiluminescence characteristics, including CH, for CH_4/NH_3 flames. Interestingly, however, in the CH_4/NH_3 blends they studied, the CH* chemiluminescence intensity peak was located on the slightly fuel rich side, around $\Phi = 1.0 - 1.1$, showing a different trend from the results of the present study. This newly suggests the possibility that the characteristics are altered because OH, O_2, and O, which are necessary for CH* formation, are also consumed by and compete with oxidation reactions originating from NH_3, H_2, and CO in the fuel.

3.4. Chemical reactor network analysis

A graph plotting the CRN calculation results and experimental results for NO and CO concentrations under various conditions where X_{NH3} was changed at $\Phi = 1.0$ is shown in Fig. 9 (a). The calculation results using GRI-Mech 3.0 [46] clearly over predicted the NO and CO concentrations compared to the experimental results at $X_{NH3} = 0.6$, and the calculation did not converge at high X_{NH3}, making it impossible to obtain results. The CRN calculation results using the mechanisms of Okafor et al. [47] and Li et al. [48] showed similar trends to each other, but differed significantly to GRI-Mech 3.0. For NO concentration, both mechanisms slightly over predicted the concentration at $X_{NH3} = 0.9$, but showed good agreement with the experimental results at $X_{NH3} = 0.6$ and 0.8. For CO concentration, although slightly over-predicted at $X_{NH3} = 0.6$, they were able to predict the low values under high X_{NH3} conditions. Therefore, these results indicate that more work is needed to improve mechanisms for predicting COG/NH_3 blends with high X_{NH3} blends.

Furthermore, experimental data and CRN calculation results from each mechanism, for cases where the equivalence ratio was varied in the range of $\Phi = 0.9$–1.1 at $X_{NH3} = 0.6$, are shown in Fig. 9 (b). Although the calculations with GRI-Mech 3.0 [46] converged for all equivalence ratio conditions, it was found that the NO concentration was overestimated, particularly at $\Phi = 0.9$. The mechanism by Okafor et al. [47] failed to converge at $\Phi = 0.9$, revealing an issue with its stability. The mechanism by Li et al. [48], however, demonstrated higher accuracy and computational stability compared to the other two mechanisms, thus confirming the validity of its adoption for the CRN study.

3.4.1. Key reactions of NO consumption and production

The ROP and Sensitivity, respectively, for the production and consumption of NO at $\Phi = 1.0$ for $X_{NH3} = 0.6$ and 0.8 are shown in Figs. 10 and 11. To facilitate the discussion of the main reactions in each blend, the ROP was normalised by the maximum absolute value for each blend.

First, the ROP results (Fig. 10) revealed that for NO consumption, $NH + NO \leftrightarrow N_2O + H$ is the most dominant reaction under all conditions,

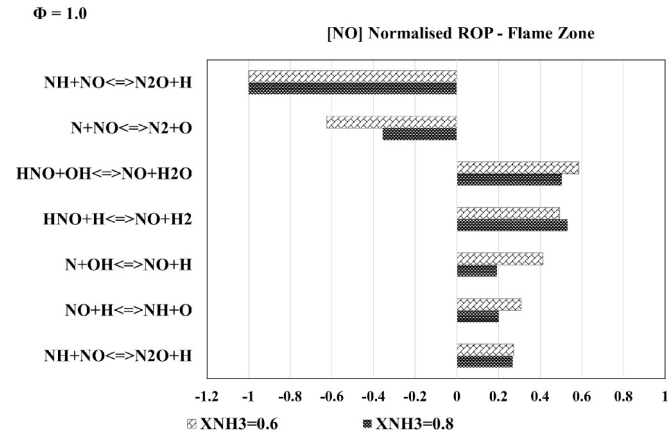

Fig. 10. Flame zone normalised ROP for the significant NO reactions at $\Phi = 1.0$ for $X_{NH3} = 0.6$ and 0.8.

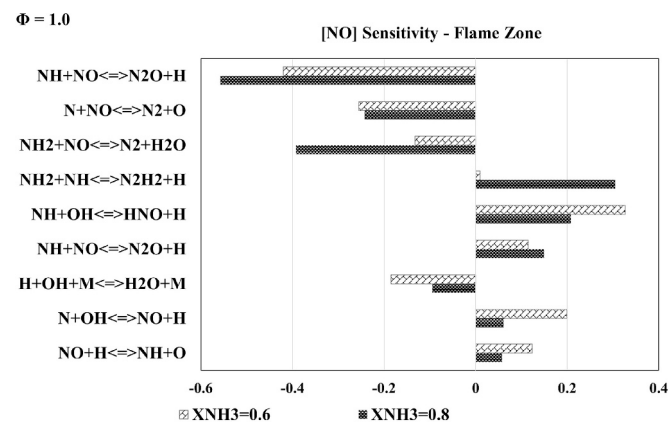

Fig. 11. Flame zone sensitivity at $\Phi = 1.0$ for $X_{NH3} = 0.6$ and 0.8.

and the consumption contribution of the next dominant reaction, $N + NO \leftrightarrow N_2 + O$, decreases as X_{NH3} increases. This trend is consistent with previous studies on H_2/NH_3 blends [58], suggesting that the main reactions for NO consumption are the same in COG/NH_3 combustion. In contrast, for NO production reactions, $HNO + OH \leftrightarrow NO + H_2O$ was found to be the most dominant at $X_{NH3} = 0.6$. While this reaction has been included in the top lists of previous ROP analyses for ammonia combustion under fuel lean conditions [58–60], it has never been dominant under stoichiometric conditions based on the available

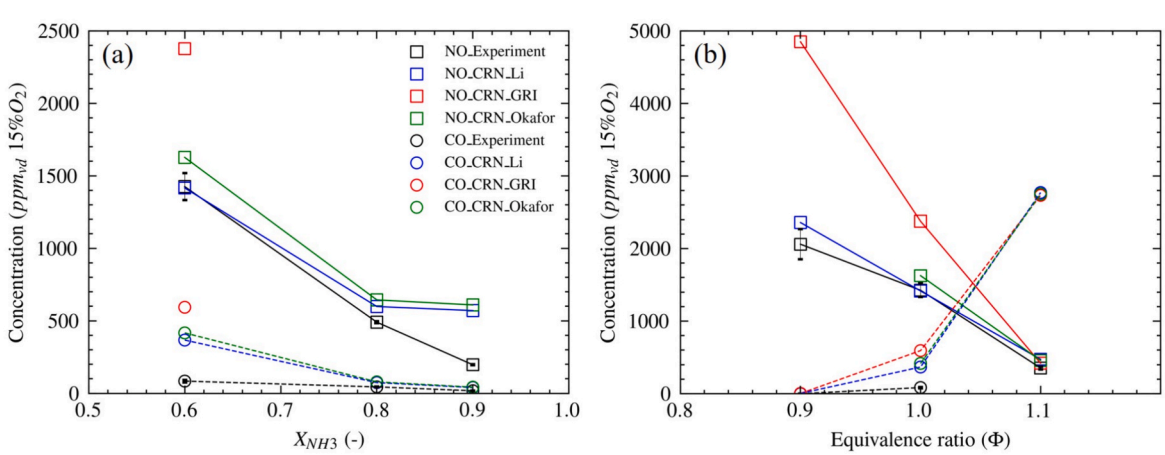

Fig. 9. Comparison of experimental and CRN predicted NO and CO concentration at (a) $\Phi = 1.0$ and (b) $X_{NH3} = 0.6$.

literature. Therefore, it has been newly identified that this reaction is crucial for understanding COG/NH_3 combustion. At $X_{NH3} = 0.8$, which has a high NH_3 fraction, HNO + H ↔ NO + H_2 is the most dominant reaction, consistent with previous findings [58]. Consequently, the emergence of HNO + OH ↔ NO + H_2O at low X_{NH3} is likely to be caused by the increased abundance of OH in the combustion zone due to the presence of COG (particularly H_2, CH_4, and CO). Furthermore, Fig. 10 indicates that the influence of the reaction N + OH ↔ NO + H increases at $X_{NH3} = 0.6$. Since this is a Zeldovich reaction, which is a representative reaction for thermal NOx, it is inferred that the rise in flame temperature [61] due to the lower X_{NH3} contributes to the increase in NO concentration shown in Fig. 6(a).

Next, the sensitivity analysis results (Fig. 11) revealed that for NO consumption, the main consumption reactions identified in the ROP analysis are themselves highly influential. In addition, at high X_{NH3}, the reduction of NO by NH_2, which is abundant in the combustion field, was also found to significantly affect NO consumption. Furthermore, regarding NO production at $X_{NH3} = 0.6$, the reaction NH + OH ↔ HNO + H, which is related to the OH and HNO in the main production reaction (HNO + OH ↔ NO + H_2O), was found to have a large influence. Moreover, at $X_{NH3} = 0.8$, the reaction NH_2 + NH ↔ N_2H_2 + H, which involves NH_2 and NH (abundant at high X_{NH3}) and H (involved in the main NO production reaction, HNO + H ↔ NO + H_2), was also shown to have a significant impact.

This analysis indicates that for NO consumption and production, while competition between reactions involving OH and H is conceivable, the direct influence of reactions involving carbon (C) from CH_4 and CO appears to be minor.

3.4.2. Key reactions of CO consumption and production

The ROP and Sensitivity, respectively, for the production and consumption of CO at Φ = 1.0 for $X_{NH3} = 0.6$ and 0.8 are shown in Figs.12 and 13. To facilitate the discussion of the main reactions in each blend, the ROP was normalised by the maximum absolute value for each blend.

First, the ROP results (Fig. 12) revealed that CO consumption is dominated by OH, which is consistent with previous research findings for conventional hydrocarbons [62]. Furthermore, for CO production at Φ = 1.0, the decomposition of HCO was found to be dominant, similar to conventional fuels [62]. However, a new finding is that the reaction NCO + H ↔ NH + CO, which results from the presence of ammonia, contributes slightly to CO production under high X_{NH3} conditions.

Next, the sensitivity analysis results (Fig. 13) indicated that for CO consumption, the reaction H + O_2 ↔ O + OH, which involves the OH radical used in consumption, has a greater influence than the consumption reaction itself (CO + OH ↔ CO_2 + H). Regarding CO production, the reaction NH + OH ↔ HNO + H has a significant impact.

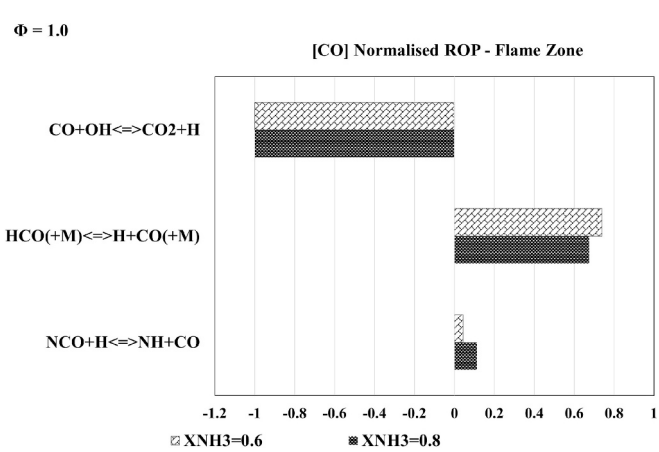

Fig. 12. Flame zone normalised ROP for the significant CO reactions at Φ = 1.0 for $X_{NH3} = 0.6$ and 0.8.

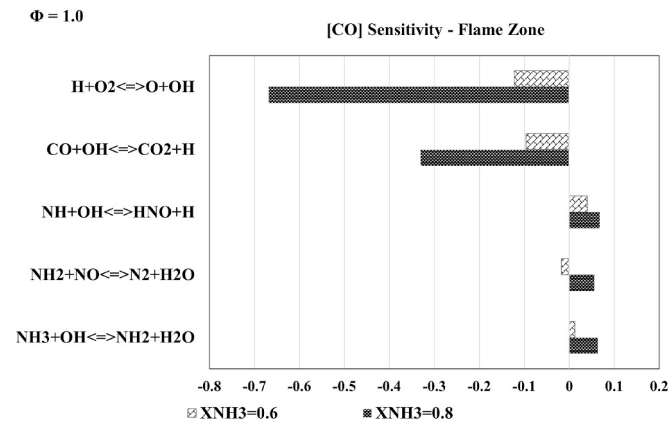

Fig. 13. Flame zone sensitivity at Φ = 1.0 for $X_{NH3} = 0.6$ and 0.8.

This suggests that the H produced by this reaction has an inhibitory effect on the decomposition of HCO, which also produces H. As mentioned earlier, this reaction also has a major influence on NO production, revealing it to be a key reaction that affects the formation of both harmful NO and CO in COG/NH_3 blend combustion. Additionally, it has become clear that NH_2 + NO ↔ N_2 + H2O and NH_3 + OH ↔ NH_2 + H_2O, which involve NH_2 produced during the initial decomposition and NH_3 itself, affect CO formation, particularly under high X_{NH3} conditions. This result further suggests the competition for OH discussed before; it is thought that NH_3 consumes OH under high X_{NH3} conditions, thereby inhibiting CO consumption. The data in Fig. 6(e) shows that as the equivalence ratio increases, the CO concentration rises sharply due to unburned CO slip, which surpasses the CO consumption suppression effect at high X_{NH3}. However, the fact that there is a certain degree of CO consumption suppression under high X_{NH3} conditions around Φ = 1.0, where both NO and CO concentrations are low, is a crucial finding for controlling emissions in practical applications.

4. Conclusions

This study provides the first comprehensive experimental and kinetic analysis of COG/NH_3 premixed swirl flames. A key novel finding is the demonstration of a synergistic relationship that dramatically enhances combustion stability. Contrary to the individual fuel characteristics of flashback-prone COG and blow-off-prone ammonia, their blending resulted in a significantly wider and more practical operational window, with the maximum range observed at $X_{NH3} = 0.2$.

Furthermore, this work offers unprecedented insights into the pollutant formation mechanisms. For the first time in the literature concerning stoichiometric ammonia blend combustion, HNO + OH ↔ NO + H_2O was identified as a dominant NO production reaction. This critical pathway is uniquely promoted by the abundance of OH radicals originating from the COG components, a mechanism not prevalent in other ammonia fuel blends.

The study also uniquely identifies the NH + OH ↔ HNO + H reaction as a pivotal hub influencing both NO and CO formation, revealing a complex interplay between nitrogen and carbon chemistry.

In conclusion, the fundamental data and new chemical kinetic insights generated by this research are valuable for future progress. They establish a robust foundation for the design of next-generation industrial burners, offering essential data and insights for the refinement and validation of CFD models for this promising low-carbon fuel. This work ultimately accelerates the development of COG/NH_3 co-firing technology as a tangible decarbonisation strategy for the steel industry.

CRediT authorship contribution statement

Daisuke Sato: Writing – original draft, Visualization, Project

administration, Methodology, Investigation, Data curation. **Jordan Davies:** Writing – review & editing, Investigation, Data curation. **Sanggak Lee:** Investigation. **Syed Mashruk:** Writing – review & editing, Supervision. **Agustin Valera-Medina:** Writing – review & editing, Supervision. **Ryoichi Kurose:** Writing – review & editing, Supervision.

Declaration of competing interest

The authors declare that they have no known competing financial interests or personal relationships that could have appeared to influence the work reported in this paper.

Acknowledgements

The work was supported by Project AMBURN with funding from the Department for Energy Security & Net Zero (DESNZ) under award no. IFS2-06-FLO, EPSRC SAFE AGT (EP/T009314/1) and Nippon Steel Corporation. The experimental work was undertaken at Cardiff University's Thermofluids lab (W/0.17) with invaluable technical support from Mr. Jonathan Martin.

Data availability

Supplementary material will be provided at the later stage of the submission. Information on the data underpinning the results presented here, including how to access them, can be found in the Cardiff University data catalog at https://doi.org/10.17035/cardiff.30234904.

References

[1] Razzaq R, Li C, Zhang S. Coke oven gas: Availability, properties, purification, and utilization in China. Fuel 2013;113:287–99.
[2] Modesto M, Nebra SA. Exergoeconomic analysis of the power generation system using blast furnace and coke oven gas in a Brazilian steel mill. Appl Therm Eng 2009;29:2127–36.
[3] Valera-Medina A, Roldan A. Ammonia from Steelworks. In: Boddula R, Asiri AM, editors. Inamuddin. Sustainable Ammonia Production, Cham: Springer International Publishing; 2020. p. 69–80.
[4] Pugh D, Crayford AP, Bowen PJ, O'Doherty T, Marsh R, Steer J. Laminar flame speed and markstein length characterisation of steelworks gas blends. Appl Energy 2014;136:1026–34.
[5] Zhai Y, Wang S, Wang Z, Zhang T, Ji C. Experimental and numerical study on laminar combustion characteristics of by-product hydrogen coke oven gas. Energy 2023;278:127766.
[6] Li J, Ma L, Qu P, Tian B, Nie Y, Liu L, et al. Comparative life cycle assessment of ammonia production by coke oven gas via single and coproduction processes. Sci Total Environ 2023;882:163638.
[7] Zhang Y, Liu H, Li J, Deng Y, Miao X, Xu D, et al. Life cycle assessment of ammonia synthesis in China. Int J Life Cycle Assess 2022;27:50–61.
[8] Zhang Y, Tian Z, Chen X, Xu X. Technology-environment-economy assessment of high-quality utilization routes for coke oven gas. Int J Hydrogen Energy 2022;47:666–85.
[9] Best available techniques (BAT) reference document for iron and Steel Production: Industrial emissions Directive 2010/75/EU : Integrated pollution prevention and control$nElektronische ressource. 2013.
[10] Valera-Medina A, Amer-Hatem F, Azad AK, Dedoussi IC, de Joannon M, Fernandes RX, et al. Review on Ammonia as a Potential Fuel: From Synthesis to Economics. Energy Fuels 2021;35:6964–7029.
[11] Kobayashi H, Hayakawa A, Somarathne KDKA, Okafor EC. Science and technology of ammonia combustion. Proc Combust Inst 2019;37:109–33.
[12] Elbaz AM, Wang S, Guiberti TF, Roberts WL. Review on the recent advances on ammonia combustion from the fundamentals to the applications. Fuel Communications 2022;10:100053.
[13] Mashruk S, Shi H, Mazzotta L, Ustun CE, Aravind B, Meloni R, et al. Perspectives on NO X emissions and impacts from ammonia combustion processes. Energy Fuels 2024;38:19253–92.
[14] Kekul O, Ilbas M, Arslan B. Numerical investigation of the laminar burning velocity and adiabatic flame temperature phenomenon for NH 3 /Hydrogen rich coal gases (HRCGs)/air flames. Energy Sources Recovery Util Environ Eff 2024;46:10579–98.
[15] Awad OI, Zhou B, Harrath K, Kadirgama K. Characteristics of NH3/H2 blend as carbon-free fuels: A review. Int J Hydrogen Energy 2023;48:38077–100.
[16] Li J, Huang H, Kobayashi N, He Z, Nagai Y. Study on using hydrogen and ammonia as fuels: Combustion characteristics and NOx formation. Int J Energy Res 2014;38:1214–23.
[17] Ichikawa A, Hayakawa A, Kitagawa Y, Kunkuma Amila Somarathne KD, Kudo T, Kobayashi H. Laminar burning velocity and Markstein length of ammonia/hydrogen/air premixed flames at elevated pressures. Int J Hydrogen Energy 2015;40:9570–8.
[18] Chen X, Liu Q, Zhao W, Li R, Zhang Q, Mou Z. Experimental and chemical kinetic study on the flame propagation characteristics of ammonia/hydrogen/air mixtures. Fuel (Lond) 2023;334:126509.
[19] Hussein NA, Valera-Medina A, Alsaegh AS. Ammonia- hydrogen combustion in a swirl burner with reduction of NOx emissions. Energy Procedia 2019;158:2305–10.
[20] Nawaz B, Nasim MN, Das SK, Landis J, SubLaban A, Trelles JP, et al. Combustion characteristics and emissions of nitrogen oxides (NO, NO2, N2O) from spherically expanding laminar flames of ammonia–hydrogen blends. Int J Hydrogen Energy 2024;65:164–76.
[21] Sato D, Davies J, Mazzotta L, Mashruk S, Valera-Medina A, Kurose R. Effects of Reynolds number and ammonia fraction on combustion characteristics of premixed ammonia-hydrogen-air swirling flames. Proc Combust Inst 2024;40:105283.
[22] Tu Y, Xu S, Liu H. Combustion and emission characteristics of NH3/CH4/air in a model swirl combustor: Comparison between premixed and non-premixed modes. Int J Hydrogen Energy 2023. https://doi.org/10.1016/j.ijhydene.2023.01.235.
[23] Zhang M, An Z, Wei X, Wang J, Huang Z, Tan H. Emission analysis of the CH4/NH3/air co-firing fuels in a model combustor. Fuel 2021;291:120135.
[24] Sun J, Yang Q, Zhao N, Chen M, Zheng H. Numerically study of CH4/NH3 combustion characteristics in an industrial gas turbine combustor based on a reduced mechanism. Fuel (Lond) 2022;327:124897.
[25] An Z, Zhang M, Zhang W, Mao R, Wei X, Wang J, et al. Emission prediction and analysis on CH4/NH3/air swirl flames with LES-FGM method. Fuel (Lond) 2021;304:121370.
[26] Khateeb AA, Guiberti TF, Wang G, Boyette WR, Younes M, Jamal A, et al. Stability limits and NO emissions of premixed swirl ammonia-air flames enriched with hydrogen or methane at elevated pressures. Int J Hydrogen Energy 2021;46:11969–81.
[27] Han X, Wang Z, Costa M, Sun Z, He Y, Cen K. Experimental and kinetic modeling study of laminar burning velocities of NH3/air, NH3/H2/air, NH3/CO/air and NH3/CH4/air premixed flames. Combust Flame 2019;206:214–26.
[28] Yang X, Deng H, Yu C, Shi X, Song J, Zhu Q, et al. Study of laminar burning velocity and flame instability of NH3/coke oven gas/air premixed flame at elevated temperature and pressure. Int J Hydrogen Energy 2025;128:236–47.
[29] Hewlett SG, Pugh DG, Valera-Medina A, Giles A, Runyon J, Goktepe B, et al. Industrial wastewater as an enabler of green ammonia to power via gas turbine technology. Volume 3: Ceramics; Coal, Biomass, Hydrogen, and Alternative Fuels, American Society of Mechanical Engineers; 2020, p. V003T03A006.
[30] Hewlett SG, Valera-Medina A, Pugh DG, Bowen PJ. Gas Turbine Co-Firing of Steelworks Ammonia With Coke Oven Gas or Methane: A Fundamental and Cycle Analysis. ASME Turbo Expo 2019: Turbomachinery Technical Conference and Exposition 2019:V003T03A018.
[31] Mashruk S, Okafor EC, Kovaleva M, Alnasif A, Pugh D, Hayakawa A, et al. Evolution of N2O production at lean combustion condition in NH3/H2/air premixed swirling flames. Combust Flame 2022;244:112299.
[32] British Standards Institute. British Standard ISO 11042-1:1996, gas turbines. Exhaust gas emission measurement and evaluation. 1996.
[33] Cheng Q, Karimkashi S, Ahmad Z, Kaario O, Vuorinen V, Larmi M. Hyperspectral image reconstruction from colored natural flame luminosity imaging in a tri-fuel optical engine. Sci Rep 2023;13:2445.
[34] Gore JPP, Mahoney EJD, Smith JA, Ashfold MNR, Mankelevich YA. Imaging and modeling C2 radical emissions from microwave plasma-activated methane/hydrogen gas mixtures: Contributions from chemiluminescent reactions and investigations of higher-pressure effects and plasma constriction. J Phys Chem A 2021;125:4184–99.
[35] Ikeda Y, Kojima J, Nakajima T, Akamatsu F, Katsuki M. Measurement of the local flamefront structure of turbulent premixed flames by local chemiluminescence. Proc Combust Inst 2000;28:343–50.
[36] Devriendt K, Look HV, Ceursters B, Peeters J. Kinetics of formation of chemiluminescent CH(A2Δ) by the elementary reactions of C2H(X2 Σ+) with O (3P) and O2(X3Σg−): A pulse laser photolysis study. Chemical Physics Letters 1996;261:450–6.
[37] Gaydon A. The spectroscopy of flames 2012.
[38] Zhu X, Roberts WL, Guiberti TF. UV-visible chemiluminescence signature of laminar ammonia-hydrogen-air flames. Proc Combust Inst 2023;39:4227–35.
[39] Mashruk S, Zhu X, Roberts WL, Guiberti TF, Valera-Medina A. Chemiluminescent footprint of premixed ammonia-methane-air swirling flames. Proc Combust Inst 2023;39:1415–23.
[40] Dasch CJ. One-dimensional tomography: a comparison of Abel, onion-peeling, and filtered backprojection methods. Appl Opt 1992;31:1146–52.
[41] Mashruk S, Xiao H, Pugh D, Chiong MC. Numerical Analysis on the Evolution of NH2 in Ammonia/hydrogen Swirling Flames and Detailed Sensitivity Analysis under Elevated Conditions. Combust Sci Technol 2023.
[42] Davies J, Mashruk S, Sato D, Mazzotta L, Pugh D, Valera-Medina A. Emissions analyses of humidified cracked ammonia swirling flames. Combust Flame 2025;274:113984.
[43] Mashruk S, Kovaleva M, Alnasif A, Chong CT, Hayakawa A, Okafor EC, et al. Nitrogen oxide emissions analyses in ammonia/hydrogen/air premixed swirling flames. Energy 2022;260:125183.
[44] Almarzooq YM, Hay MK, Khan-Ghauri M, Mathieu O, Kulatilaka W, Petersen E. The effect of mixture variation and initial temperature on the NH2* thickness of spherically propagating laminar ammonia flames. J Eng Gas Turbine Power 2024;146:121006.
[45] Karan A, Dayma G, Chauveau C, Halter F. Insight into the inner structure of stretched premixed ammonia-air flames. Proc Combust Inst 2023;39:1743–52.

[46] Frenklach M, Moriarty NW, Eiteneer B, Goldenberg M. GRI-Mech version 1999;3.
[47] Okafor EC, Naito Y, Colson S, Ichikawa A, Kudo T, Hayakawa A, et al. Experimental and numerical study of the laminar burning velocity of CH4–NH3–air premixed flames. Combust Flame 2018;187:185–98.
[48] Li Y, Zhang Y, Fang J, Xi Z, Zhang J, Liu Z, et al. Combustion enhancement of ammonia by co-firing dimethyl ether/hydrogen mixtures under methane-equivalent calorific value. Combust Flame 2024;265:113490.
[49] Mashruk S, Alnasif A, Yu C, Thatcher J, Rudman J, Peronski L, et al. Combustion characteristics of a novel ammonia combustor equipped with stratified injection for low emissions. Journal of Ammonia Energy 2023;1:21–32.
[50] Lai S, Chen D, Zhang J, Xie Y, Fan M, Li X, et al. Blow-off limits, flame structure, and emission characteristics of lean partially premixed swirl-stabilized flames with NH3/CH4. Energy Fuels 2024;38:4721–32.
[51] Liu Z, Bin S, Chen S, Jiang J, Zhang Y, Shi X, et al. Insights into combustion and emission characteristics of ammonia co-firing with hydrogen-rich gas for gas turbine applications. Energy (Oxf) 2025;324:135967.
[52] Mazzotta L, Zhu X, Davies J, Sato D, Borello D, Mashruk S, et al. Assessing the potential of a chemiluminescence and machine learning-based method for the sensing of premixed ammonia–hydrogen–air turbulent flames. Int J Hydrogen Energy 2025;100:945–54.
[53] Karan A, Dayma G, Khan-Ghauri M, Mathieu O, Petersen EL, Chauveau C, et al. Investigating the role of NH2* as an indicator of preferential diffusion effects in premixed NH3/air flames. Fuel (Lond) 2025;395:135139.
[54] Pugh D, Runyon J, Bowen P, Giles A, Valera-Medina A, Marsh R, et al. An investigation of ammonia primary flame combustor concepts for emissions reduction with OH*, NH2* and NH* chemiluminescence at elevated conditions. Proc Combust Inst 2021;38:6451–9.
[55] Su H, Wu Y, Yan J, Jiang L. Experimental study on chemiluminescence properties of ammonia-methane non-premixed laminar flames. Energies 2025;18:402.
[56] Tian X, Gong Y, Guo Q, Wu J, Yu G. Investigation of C2* chemiluminescence based on improved CH4/O2 diffusion flame combustion reaction mechanism. Combust Flame 2024;265:113511.
[57] Zhu X, Khateeb AA, Roberts WL, Guiberti TF. Chemiluminescence signature of premixed ammonia-methane-air flames. Combust Flame 2021;231:111508.
[58] Alnasif A, Mashruk S, Hayashi M, Jójka J, Shi H. Performance investigation of currently available reaction mechanisms in the estimation of NO measurements: a comparative study. Energies 2023.
[59] Nakamura H, Hasegawa S, Tezuka T. Kinetic modeling of ammonia/air weak flames in a micro flow reactor with a controlled temperature profile. Combust Flame 2017;185:16–27.
[60] Glarborg P. The NH3/NO2/O2 system: Constraining key steps in ammonia ignition and N2O formation. Combust Flame 2023;257:112311.
[61] Sato D, Davies J, Lee S, Mashruk S, Valera-Medina A, Kurose R. Radiative characteristics of premixed Coke Oven Gas-Ammonia swirling flames. Fuel (Lond) 2025;401:135741.
[62] Westbrook CK, Dryer FL. Chemical kinetic modeling of hydrocarbon combustion. Progress in Energy and Combustion Science 1984;10:1–57.